



Effect of Temperature on the Electrochemical Corrosion Behavior of X80 Steel in Silty Soil Containing Sodium Chloride

Xiangling Bai, Bin He, Pengju Han , Ruizhen Xie, Funan Sun, Zhiwei Chen, Xinyu Liu, and Yuting Wang

Submitted: 2 June 2021 / Revised: 22 July 2021 / Accepted: 12 August 2021 / Published online: 17 September 2021

The corrosion behavior of X80 pipeline steel in silty soil containing chloride ions at different temperatures was investigated using different electrochemical techniques. Scanning electron microscopy and energy-dispersive spectroscopy were used to characterize the corrosion morphology and physicochemical properties of the X80 steel. The lower chloride ion concentration and the ambient temperature were associated with the lower the unfrozen water content in the soil and the easier it to form an anoxic corrosion environment. As the chloride ion concentration increased, the corrosion rate increased at $-10\text{ }^{\circ}\text{C}$ and first increased and then decreased at $-20\text{ }^{\circ}\text{C}$. The steel corroded surface were present irregular elliptical uncorroded areas in a soil environment at the sub-zero temperature, which may be caused by the liquid–solid phase transition hindering the transportation of the reducing medium. The rust layers in a positive temperature soil environment were present relatively dry. This phenomenon is due to the current density is high, and the exothermic process is evident.

Keywords corrosion rate, electrochemical, saline silty soil, temperature, X80 steel

1. Introduction

Conservation and management of oil and gas pipelines play a critical role in the construction of the country, the stability of the society and the safety of people. After the oil and gas pipelines are laid underground, their service environment system can be classified into internal and external environments, according to the space position separated by the pipe wall. Among them, the pipe wall, its internal surface conditions, all the substances in the pipeline and their physical and chemical states can be considered the internal environment (Ref 1, 2). The pipe wall and its external surface conditions and all the substances surrounding the pipeline and their physical and chemical states can be considered external environments (Ref 3). Because the outer surface of the oil and gas pipeline will suffer varying levels of corrosion from soil and groundwater, the corrosion area is comprehensive, and the corrosion consequences are significant.

Soil is one of the essential elements of the ecosystem and the ultimate receptor of pollutants. The pollution is mainly caused by pollutants following atmospheric dust fall, water migration and solid waste storage. Soil pollution has the characteristics of concealment, hysteresis and accumulation. Once contaminated,

the governance difficulty and cost are often more incredible than air pollution and water pollution (Ref 4, 5). Soil corrosion of buried oil and gas pipelines refers to the phenomenon that varying reducing media in the soil environment causes different degrees of corrosion and damage to the pipelines. It is one of the major causes of the leakage of buried oil and gas pipelines. More recently, scholars have conducted much research on various factors that cause corrosion behavior in the soil environment, including soil pH (Ref 6), soil moisture content (Ref 7, 8), soil layer thickness (Ref 9), DC interference voltage (Ref 10), soil bacterial microbial corrosion (Ref 11, 12), stress corrosion cracking (Ref 13) and temperature and humidity effects (Ref 14, 15). Moreover, the steel corrosion failure impacts of soil salinity cannot be ignored. Shanxi Province has become one of the China's most important oil and gas pipeline hubs with its abundant coal-bed methane resources. It undertakes the formidable task of ensuring oil and natural gas transportation in the capital Beijing and even the whole country. All the time, guarantee the stable operation of the pipeline is its task. Our research group have previously collected soil physical and chemical properties in Shanxi Province through Shanxi Survey Design Institute and Shanxi Academy of Building Research to obtain a total of 2442 points of data collected. Soil information is mainly from the soil analysis results table. The descriptive statistical analysis and correlation analysis on soil data in Shanxi Province have been performed using SPSS Statistics software. It is shown that the soil in Shanxi Province is commonly weakly alkaline soil, with a pH range from 7.0 to 9.8. The Cl^- and SO_4^{2-} in the soil are widely spatial distributed and have substantial variability.

In pipeline construction, it is essential to strengthening the feasibility demonstration and safety audit of the particularity soil in the pipeline service area. Therefore, conducting the soil corrosion study will effectively ensure the safety of the pipeline. Currently, a variety of methods exist to study soil corrosion: on-site measurement method, integrated evaluation

Xiangling Bai, Bin He, Pengju Han, Funan Sun, Zhiwei Chen, Xinyu Liu, and Yuting Wang, College of Civil Engineering, Taiyuan University of Technology, West Yingze Street 79, Taiyuan 030024, People's Republic of China; and Ruizhen Xie, Mechanics Institute, Jinzhong University, Jinzhong 030619, People's Republic of China. Contact e-mail: 13834569544@163.com.

method, laboratory simulation testing and electrochemical test method, data processing method and macroscopical and microscopical observation method of corrosion products (Ref 16, 17). Among the research methods, laboratory simulation testing and electrochemical test method are some of the most widely used. It utilizes electrochemical instruments to study the metal–soil corrosion system, uses electrochemical impedance spectroscopy and polarization curve graphs to simulate equivalent circuits, and applies fitting software to fit parameters. It could speedily and accurately determine the corrosion rate and self-corrosion potential of metal specimens in various soil environments and analyze the corrosion mechanism.

At present, the method of anticorrosion coatings combined with cathodic protection has been applied against pipeline corrosion. Similarly, several studies point out that metal corrosion undercoating rupture is similar to natural corrosion directly exposed to a corrosive environment (Ref 18). There are multiple corrosion forms, such as uniform corrosion, pitting corrosion and microbial corrosion. In the meantime, X80 pipeline steel has widely been used for buried oil and gas pipeline transportation due to the good tensile strength. Therefore, scholars have conducted much research on the corrosion behavior of X80 steel in different types of soil environments. Zhang et al. (Ref 19) conducted that X80 steel exhibits self-passivation behavior in a simulated soil solution containing Na_2CO_3 . The protective properties of the passive film on the steel surface increased, and the corrosion rate decreased with a higher concentration in the soil solution. The anodic polarization curve shows the activation and passivation process with two anodic peaks. Wu et al. (Ref 20) analyzed that the corrosion rate of X80 steel in acidic soil environments with different positive temperatures. The corrosion rate increases with the increase in the soil environment temperature, and the polarization curve showed that the activation polarization process controlled the corrosion. Accordingly, studying the natural corrosion of X80 steel directly exposed to a corrosive environment is also of great significance for studying metal corrosion under the peeling of anticorrosive coating.

Temperature is an essential parameter in characterizing the environmental characteristics of a region. Different climatic zones, seasonal changes, soil properties and land use may affect soil temperature to different degrees. Simulating the temperature conditions that may occur is significant implications for the study of soil–steel corrosion. The minimum temperature data in Taiyuan City, Shanxi Province, China (District Station No. 53772), are obtained from the China Meteorological Data Service Centre (Ref 21). The annual change of the minimum temperature in the past decade is shown in Fig. 1 (data missing from 2016 to 2018), which shows the city's minimum temperature reached $-20.3\text{ }^\circ\text{C}$ in 2013, and the minimum temperature in other years was around $-16.5\text{ }^\circ\text{C}$. The surface meteorological observation data as public information were easily accessible from the China Meteorological Administration database. In line with these data, the first soil freezing in the soil borrowing area of Taiyuan City, Shanxi Province, began in mid- to early November. For the past decade, January had the coldest temperature, with an average temperature of $-11.9\text{ }^\circ\text{C}$. However, most previous studies of soil–steel corrosion focused on the positive temperature soil environment, and the corrosion mechanism of steel under freezing conditions of soil pore water is less explored. Hence, studies with sub-zero temperature soil corrosion environment are imperatively needed.

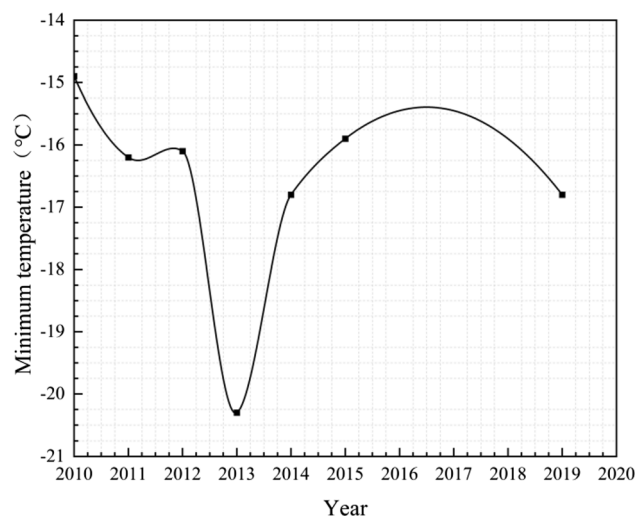


Fig. 1 Annual change of the minimum temperature in Taiyuan City

To this aim, this work uses electrochemical testing and corrosion morphology observation methods to investigate the initial corrosion behavior of silty soil containing chloride ions on X80 steel at sub-zero temperatures (-10 and $-20\text{ }^\circ\text{C}$). The corrosion mechanism was investigated based on corrosion behavior analysis. The results could provide a theoretical foundation for the construction and conservation of oil and gas pipelines in analogous regions, as well as active and practical guidance for the research and regulation of soil corrosion behavior.

2. Experimental Materials and Procedures

2.1 Materials

2.1.1 X80 Pipeline Steel Specimens. For this corrosion experiment, X80 pipeline steel material with the dimension of $10\text{ mm} \times 10\text{ mm} \times 2\text{ mm}$ was selected for the study. Its chemical compositions are listed in Table 1. Retaining the $10\text{ mm} \times 10\text{ mm}$ surface on the one side of the steel specimen as the working area, welding the copper wire to the other side and covering the non-working surface with epoxy resin. The working surface of the specimen was ground step by step from 360 grit to 1200 grit with water-resistant SiC paper on the metallographic sample grinding and polishing machine and polished with 2000 grit SiC paper. Then put the specimen into pure water for ultrasonic cleaning to remove the adsorbed material on the surface and air-dry naturally to obtain a smooth surface sample.

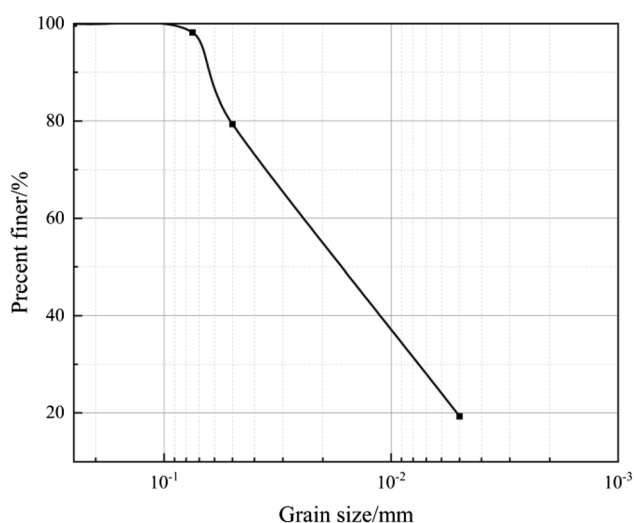
2.1.2 Soil Specimens. The soil used in this experiment was collected from a field near the buried oil and gas pipelines in Dongshan, Taiyuan City, Shanxi, China. The soil was classified as silty soil following the standards for engineering classification of soil (Ref 22), the basic physical parameters are listed in Table 2, and the cumulative particle size distribution curve is shown in Fig. 2. The soil sample was characterized using XRD (LabX XRD-6000 diffractometer made by Shimadzu, Japan) techniques to identify the mineral composition. The value of 2θ was preset as $5^\circ \sim 85^\circ$, and the step size was 0.01° . MDI Jade software was used for XRD analysis. The XRD pattern of the silty soil is shown in Fig. 3. The content of

Table 1 Chemical composition of X80 pipeline steel (wt.%)

Chemical composition	C	Mn	Si	P	S	Nb	Cu	Cr	Ni	Mo	Fe
Values, %	0.070	1.80	0.216	0.0137	0.0009	0.105	0.221	0.266	0.168	0.182	Bal.

Table 2 Basic physical parameters of the silty soil

Parameters	Values
Natural water content, %	6.79
Maximum dry density, $\text{g}\cdot\text{cm}^{-3}$	1.82
Optimum moisture content, %	15.30
Liquid limit, %	25.25
Plastic limit, %	15.6149
Plastic index	9.6351
Specific gravity	2.70

**Fig. 2** Grain size cumulative distribution curve

each mineral component determined after quantitative analysis is presented here in a tabulated form. It can be seen that the main minerals in the test silty soil are quartz (SiO_2), feldspar, calcite (CaCO_3), dolomite, amphibole and clay minerals, with quartz accounting for the highest proportion.

After the soil was naturally air-dried, crushed and passed through 1 mm sieve, washed with distilled water, stirred and stood until the separation of soil and water, measured the conductivity of the supernatant until it is the same as the conductivity of distilled water, and then separated the supernatant to obtain soil specimens. The soil specimens were put in a blast-drying oven at 105°C for 6 h and weighed after they were cooled for 30 min. The specimens were then put in the oven for another 3 h and weighed again when they were cooled to room temperature. The weighing errors between the two weights were less than 0.05 g to ensure the soil was dry. Under the condition of the maximum dry density of silty soil obtained by compaction test, using 0.90 as the compaction coefficient, the soil specimens containing different chloride ions (0.3%, 0.5%, 1% and 1.5%) under the optimal moisture content were pressed into the insulating mold box measuring $7.07\text{ cm} \times$

$7.07\text{ cm} \times 7.07\text{ cm}$ and ensured that the soil specimens are in complete contact with the X80 steel specimens. The moisture in the test soil was kept stable by wrapping and covering with waterproof breathable membrane.

2.2 Experiment Methods

The target temperatures of this study were -20 , -10 and 10°C , and the temperature was controlled by an external thermostatic bath (the model is DHC-2005-A; produced by Hangzhou Qiwei Instrument Co., LTD, China) with the error range of $\pm 0.1^\circ\text{C}$. A high-accuracy temperature sensor was inserted into the soil to record the temperature in real time. The study materials were kept at the target temperature for 24 h. CorrTest CS350 electrochemical workstation was used to conduct the electrochemical corrosion test of the X80 steel specimen. Before the electrochemical test, the power switch should be turned on to preheat for 20 min in order to make the instrument work in the state of minimum temperature drift.

2.2.1 Electrochemical Impedance Spectroscopy (EIS) Measurements. In the EIS test, the X80 steel specimen was used as the working electrode (WE), the Pt plate was used as the counter electrode (CE), and the copper/copper sulfate electrode was used as the reference electrode (RE). The distance between the three-electrode system is set closer to reduce the IR drop at the soil–steel interface (Fig. 4). In order to decrease the measurement error caused by the corrosion potential drift or the influence of the signal-to-noise ratio, a sinusoidal signal with an amplitude of 10 mV was applied, and the scanning frequency was ranging from 100,000 to 0.01 Hz. The Nyquist diagram and the Bode diagram are obtained, and the data obtained are fitted by the ZView2 software. The reliability of impedance spectroscopy is verified by checking the linearity conditions and the Kramers–Kronig conversion test to determine the conditions of causality (Ref 23).

2.2.2 Potentiodynamic Polarization Curves (PC) Measurements. Since the electrode itself needs a particular time to stabilize, before starting to test, the working electrode was polarized for 3 min at the polarization potential to eliminate the instability during the first polarization. The potential scan ranges from -0.75 to 3 V with a potential scanning rate of 1.5 mV/s . The polarization curve was obtained, and the PC data were analyzed by CVIEW2 software. The interaction equation with control variables was further obtained.

2.2.3 Morphological Characterization. After the above tests, X80 steel specimens were gently wiped with absolute ethanol to remove the loose soil particles attached to the surface. The corrosion morphology of the X80 steel surface was observed by the scanning electron microscope (SEM), and the corrosion product elements were characterized and analyzed by the energy-dispersive x-ray spectrometer (EDS) system under the working voltage of 15 kV (Hitachi High-Technologies TM3000).

All the test methods had been performed in triplicate to ensure reproducibility and reducibility.

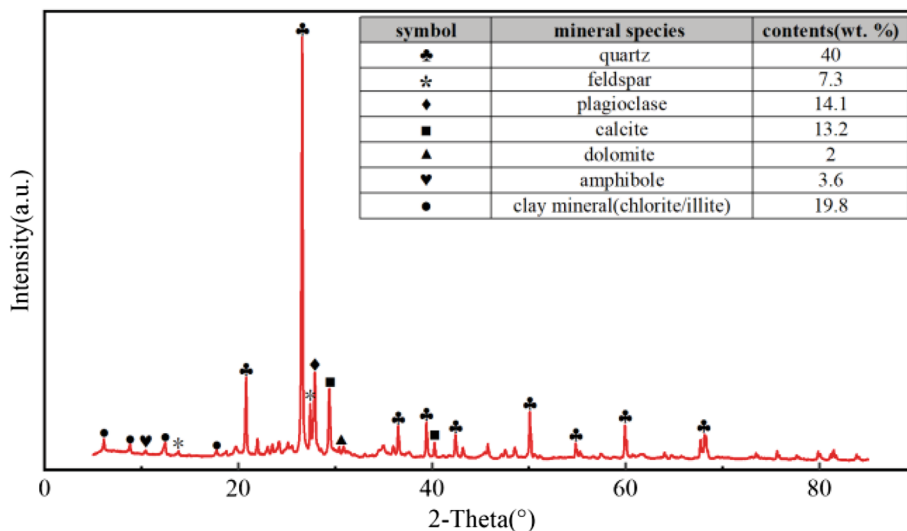


Fig. 3 XRD pattern of the silty soil

3. Results and Discussion

3.1 Impedance Behavior of X80 Steel in the Silty Soil at Various Temperatures

EIS can reflect different corrosion mechanisms: capacitance process in the high-frequency region, corrosion and dissolution process in the medium-frequency region, and induction or diffusion effects in the electrode–electrolyte interface reaction process in the low-frequency region (Ref 7). The Nyquist plots and Bode plots in the silty soil with different chloride ion concentration at various temperatures are shown in Fig 5, 6 and 7, respectively.

The Nyquist curve at $-20\text{ }^{\circ}\text{C}$ consists of high-frequency capacitor arcs, medium-frequency capacitive reactance arcs and low-frequency Warburg impedance diffusion tail arcs (see Fig. 5a). The radius of the semicircular capacitive reactance arc in the high-frequency region firstly increases and then decreases. Warburg impedance in the low-frequency region indicates that the formation of a passivation film hinders ion flow and reduces the corrosion rate. The Warburg impedance diffusion tail arc appears on the Nyquist diagram as a diffusion impedance with an angle of 45° to the real axis in a section of the low-frequency region, indicating that the deposition of corrosion products results in the interfacial corrosion reaction mainly determined by the diffusion mass transfer process. The Bode diagram at $-20\text{ }^{\circ}\text{C}$ reflects that X80 steel has the smallest impedance modulus in silt with a chloride ion concentration of 1% (see Fig. 5b).

It can be observed from the Nyquist plots that the four curves at $-10\text{ }^{\circ}\text{C}$ are consisted of high-frequency, medium-frequency and low-frequency capacitive arcs (see Fig. 6a), reflecting that the corrosion product film on the metal surface begins to dissolve, and the reducing medium in the soil penetrates into the metal surface through the corrosion product film defects, accelerating corrosion reoccurred. The radius of the capacitive reactance arc in the high-frequency region decreases with the increase in the chloride ion concentration in the silty soil. The Bode plots at $-10\text{ }^{\circ}\text{C}$ show that the impedance modulus of the X80 steel sample decreases with the increase in the ion concentration (see Fig. 6b). At a 10^{-2} HZ

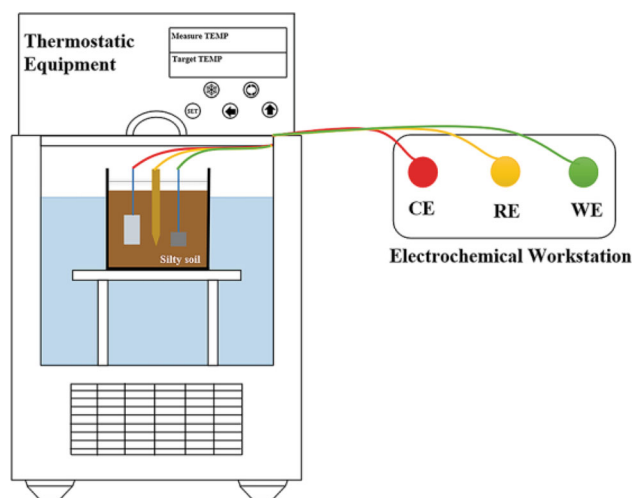


Fig. 4 Schematic diagram of three-electrode system

frequency, the impedance modulus value is more prominent at 0.3% and 0.5% concentration and more minor at 1.5% concentration.

The higher the impedance modulus in the low-frequency region was, the better the metal corrosion resistance was (Ref 24). Hence, it can be preliminary concluded that the corrosion rate of X80 steel at temperatures of -20 and $-10\text{ }^{\circ}\text{C}$ in this test concentration range is higher when the chloride ion concentration in the silty soil is 1 and 1.5%, respectively. The first time constant observed in the high-frequency region may be associated with the capacitive behavior affected by the characteristics of the soil matrix. The second time constant may be associated with the electrokinetic peculiarities of corrosion products at the soil–steel interface. The third time constant may be related to the ion adsorption and metal dissolution process of the electric double-layer distribution in the low-frequency region, and its resistance values are related to the charge transfer characteristics (Ref 25).

Figure 7(a) shows the Nyquist diagram of X80 steel when the silty soil is at a positive temperature ($10\text{ }^{\circ}\text{C}$). It can be clearly seen that the Nyquist diagrams of X80 steel tested under

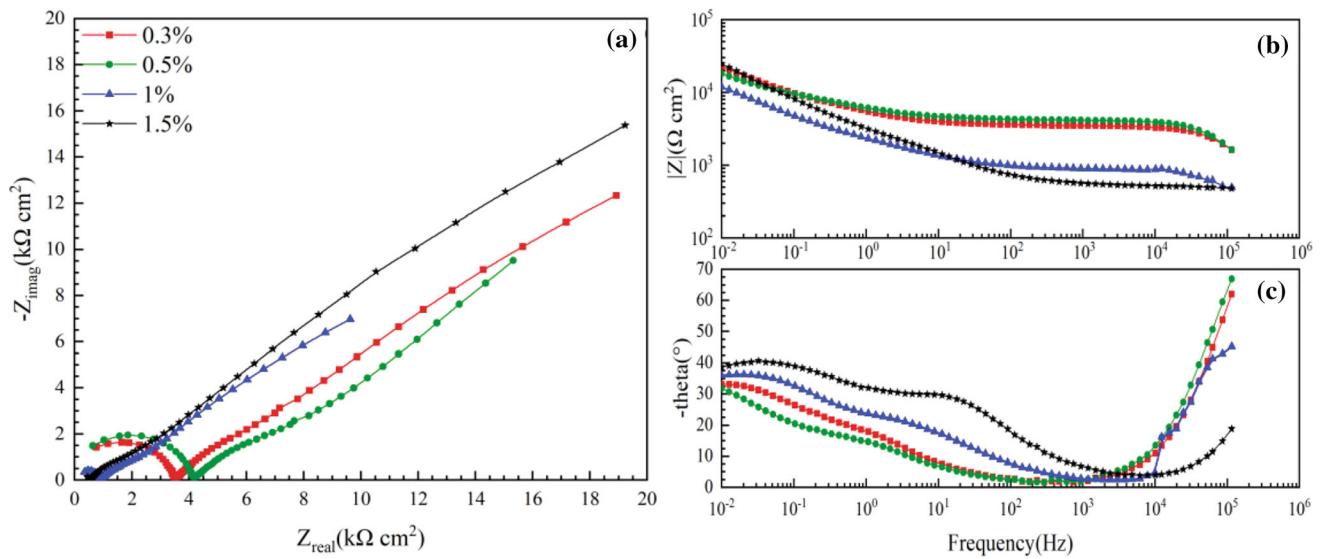


Fig. 5 EIS diagram for X80 pipeline steel in the silty soil at $-20\text{ }^{\circ}\text{C}$: (a) Nyquist plots; (b), (c) Bode plots

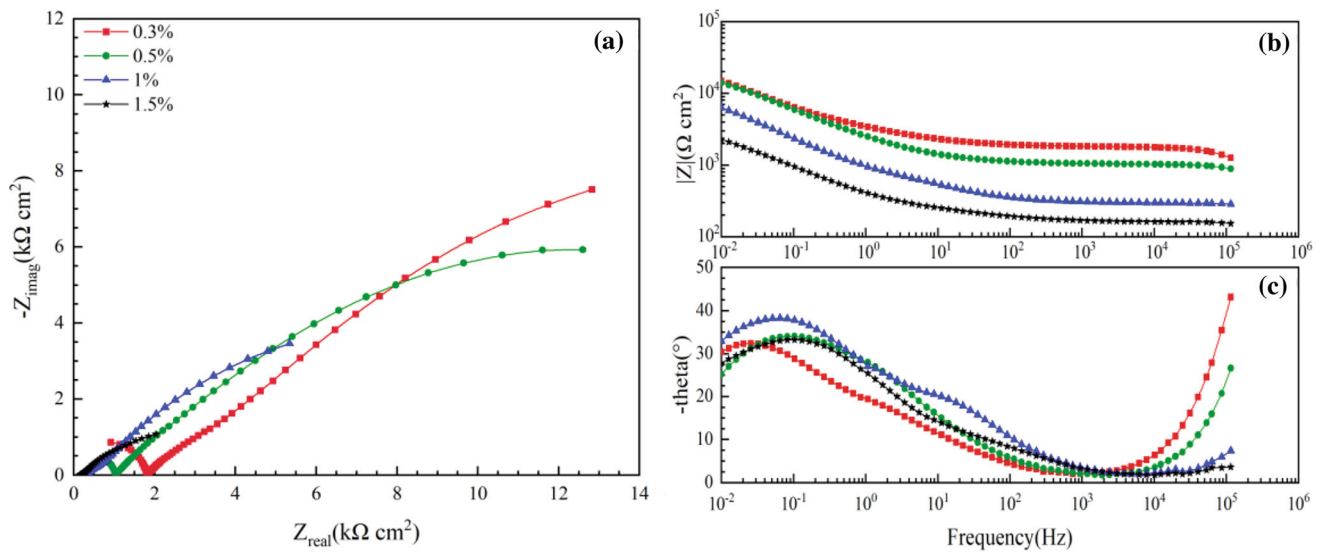


Fig. 6 EIS diagram for X80 pipeline steel in the silty soil at $-10\text{ }^{\circ}\text{C}$: (a) Nyquist plots; (b), (c) Bode plots

positive and negative temperature conditions within the concentration range of this test are significantly different. The radius of the impedance spectrum in the low-frequency region at negative temperature is larger than that at positive temperature, which reflects that the X80 steel in the negative temperature soil environment will reduce the corrosion kinetic characteristics.

The equivalent circuit model shown in the inset figure of Fig. 8 was used to fit the EIS data at negative temperature soil environment, and the fitting component values are listed in Tables 3 and 4, respectively. Among these electrochemical components, the constant phase angle element (CPE) is adopted to represent the non-ideal capacitor due to the “dispersion effect.” R_s and C_s are the resistance and capacitance of the bonding layer composed of soil particle layer, pore water layer and solid ice layer on the steel surface under negative temperature conditions, respectively. R_1 and C_1 are the resistance and capacitance of the corrosive ions of the reducing

medium in the soil penetrating the steel surface through the defects of the corrosion product film, respectively. CPE_{cp} and R_{cp} are the capacitance and resistance of the corrosion product, respectively. CPE_{dl} is electric double-layer capacitance. R_{ct} is the charge transfer resistance, and the exchange current density can be calculated. W_s is the Warburg impedance and represents the diffusion process affected by corrosion products on the surface of the steel specimens.

In this test, concentration range and the soil environment temperature are -20 and $-10\text{ }^{\circ}\text{C}$, and the first time constant value related to soil characteristics is lower in the silty soil containing 1.5 and 1% chloride ion concentration, respectively, indicating that it has high dielectric properties. Since the soil is under negative temperature, the unfrozen water content decreases with the decrease in the soil’s chloride ion concentration. With time extended, ice is gradually precipitated from the soil pore fluid until it comes into contact with the surface of the steel specimen. Due to the extremely weak conductivity of

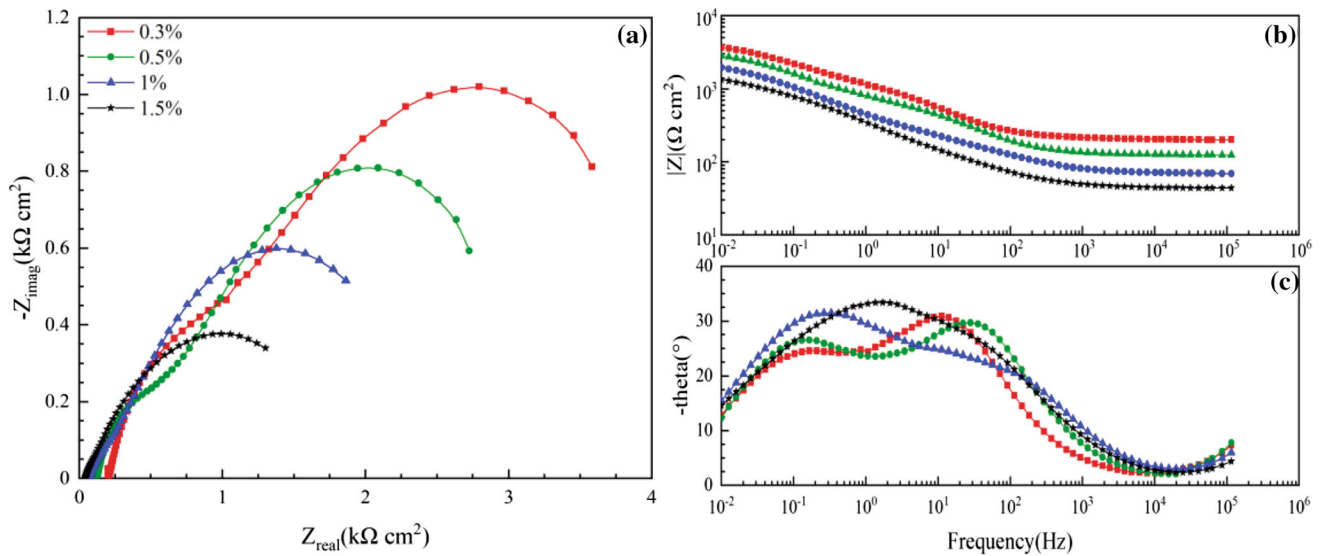


Fig. 7 EIS diagram for X80 pipeline steel in the silty soil at 10 °C: (a) Nyquist plots; (b), (c) Bode plots

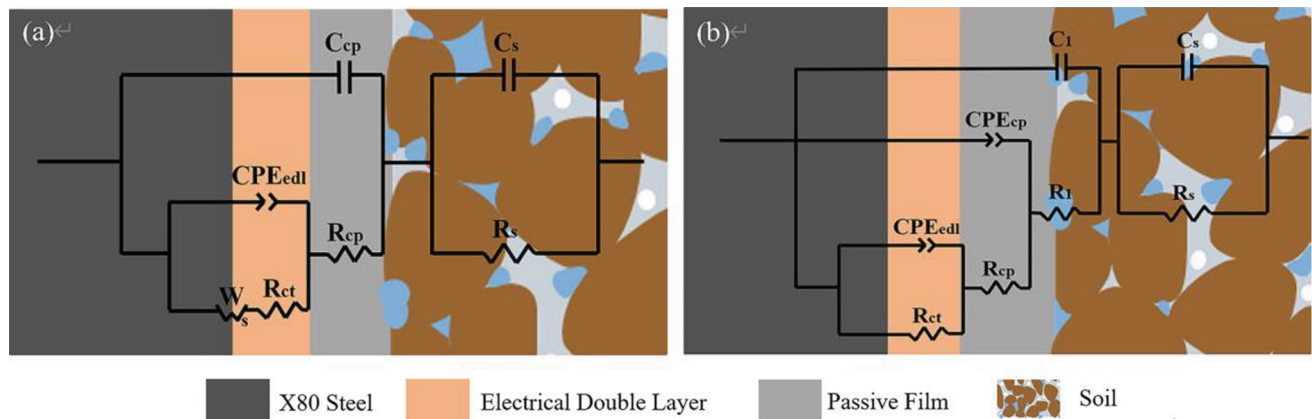


Fig. 8 Electrical equivalent circuits for (a) – 20 °C and (b) – 10 °C

Table 3 EIS fitting results of X80 pipeline steel in the silty soil at -20 °C

Cl-, mass%	Rs, Ω·cm²	Cs, F·cm⁻²	Cep, F·cm⁻²	Rcp, Ω·cm²	CPEdl-T, S·cm⁻²·s⁻ⁿ	CPEdl-P, -	Rct, Ω·cm²	W-R	W-T	W-P
0.3	294	5.19E-08	7.75E-10	3184	0.000102	0.60413	5918	44238	62.7	0.44307
0.5	344.7	5.28E-08	8.05E-10	3775	1.12E-04	0.58044	7429	65996	188.6	0.56137
1	335	2.71E-09	6.88E-09	553.8	6.20E-05	0.71061	968.4	57549	534.8	0.45508
1.5	295.6	5.45E-05	9.29E-10	498.3	0.000118	0.52224	5162	77358	29.45	0.45634

Table 4 EIS fitting results of X80 pipeline steel in the silty soil at -10 °C

Cl-, mass%	Rs, Ω·cm²	Cs, F·cm⁻²	C1, F·cm⁻²	R1, Ω·cm²	CPEcp-T, S·cm⁻²·s⁻ⁿ	CPEcp-P, -	Rcp, Ω·cm²	CPEdl-T, S·cm⁻²·s⁻ⁿ	CPEdl-P, -	Rct, Ω·cm²
0.3	118.6	6.68E-08	7.60E-10	1672	0.000141	0.54514	4578	0.000178	0.60694	36714
0.5	42	1.21E-07	6.84E-10	980.4	0.000194	0.54826	14412	0.000149	0.80463	11464
1	8.133	1.40E-06	6.15E-10	289.4	0.000151	0.6669	537.4	0.000509	0.58138	15320
1.5	130.8	6.02E-16	2.33E-08	27.13	0.000922	0.48352	298.7	0.000532	0.65826	4750

the solid ice phase, the ionization resistance of the steel specimen is increased.

The second time constant value related to corrosion product is lower in the soil containing 1% and 1.5% chloride ion concentration, which indicates that the corrosion products films have higher electroconductibility in this corrosion environment. The larger the value, the greater the barrier effect of corrosion products in the ion transport and migration process in the strongly polarized region. Surface changes of the steels and the formation of corrosion products are affected by the soil environment. The passive film produced by the corrosion behavior of X80 steel in soils with different freezing temperatures of pore water and different salt concentrations will affect the value of the time constant.

The effect of different soil environments on the structures of corrosion products film produced at the soil–steel interface is shown in Eq 1 (Ref 26):

$$\sigma = \sigma_E + \sigma_0 - \sigma_\gamma \quad (\text{Eq 1})$$

where σ is stress of the corrosion product film, which is perpendicular to the product film; σ_E is the electrostrictive stress caused by electric field around the product film; σ_0 is the soil environmental stress (Ref 27, 28); and σ_γ is the interfacial tension, which makes the corrosion product film stable, but as the corrosion process progresses, its value decreases as the thickness of the product film increases (Ref 10). In a negative temperature soil environment, the volume of the soil is swelled due to the phase transition of water and ice. Therefore, due to alters in temperature and salt ion concentration in the soil environment will alter the soil environmental stress, increasing the corrosion product film stress will have an impact on the structure of corrosion product film.

The third time constant value is related to the ion adsorption and metal dissolution process. The reciprocal of the charge transfer resistance is proportional to the corrosion rate, reflecting the corrosion rate of the metal matrix. When the soil temperature is -20 and -10 °C, its value is lower in the silt containing 1% and 1.5% chloride ion concentration, respectively, indicating that the resistance of ion transfer and transportation at the soil–steel interface is reduced and corrosion behavior is more likely to occur.

3.2 Polarization Curves of X80 Steel in the Silty Soil at Various Temperatures

X80 steel is typical dual-phase steel that contains fine ferrite phase and bainite phase, which means that the steel contains some impurities, and these sections happen to be the primary part of the electrochemical redox process, that is, the preliminary site where corrosion occurs. Steel specimens in different environmental media will also lead to altered original mechanical properties. The higher contents of Cr and Ni in the chemical composition of steel will improve its own corrosion resistance. Nevertheless, the high content of Nb will produce niobium carbide, which has an adverse effect on corrosion resistance (Ref 29). The corrosion process is the oxidation of steel and the electrochemical reduction composed of the electroactive material reduction medium and the soil structure. Figure 9 depicts the polarization curves for X80 steel specimens in the silty soil containing chloride ion concentration range of this test at -20 , -10 and 10 °C, and the corrosion kinetic parameters obtained from the curves are given in

Table 5, such as anodic and cathodic constants (B_a , B_c), corrosion potential (E_{corr}) and corrosion current density (I_{corr}).

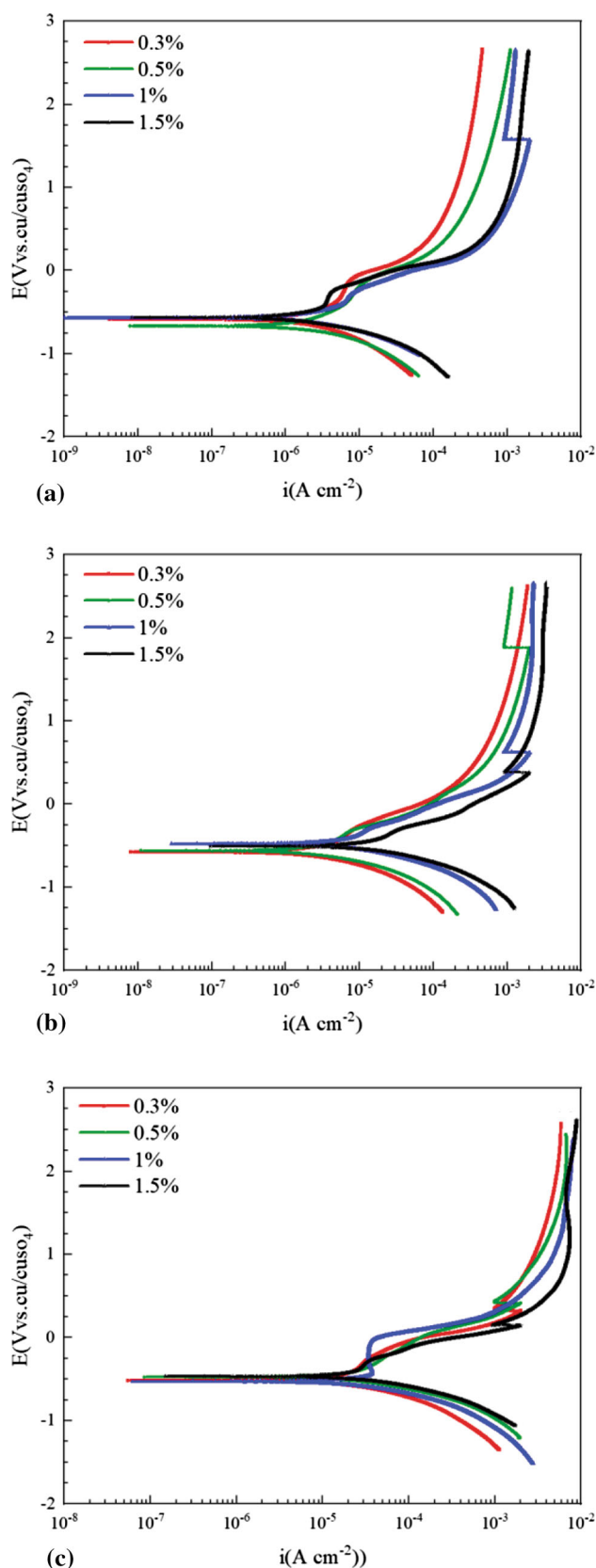


Fig. 9 Polarization curves of X80 pipeline steel in the silty soil at: (a) -20 °C; (b) -10 °C; (c) 10 °C

From the curves at the negative temperatures (see Fig. 9a and b), it can be clearly observed that the cathodic polarization curves of the steel are controlled by the activation polarization reaction, which means that the influence of the cathodic reaction of the soil electrolyte at the freezing temperature of the pore water within the concentration range of this test is negligible. At $-20\text{ }^{\circ}\text{C}$, the anodic polarization curve has a passivation region in the silty soil at a concentration of 1% (see Fig. 9a). However, when the concentration is increased to 1.5%, the curve does not show a passivation region; that is, the corrosion behavior is controlled by the activation polarization. The anodic polarization curve shifts to the right at $-10\text{ }^{\circ}\text{C}$, indicating that the anodic dissolution is accelerated (see Fig. 9b). The anodic polarization curve has a passivation phenomenon caused by the formation of corrosion product film in the silty soil at the concentration of 0.5 to 1.5%, and the membrane formed on the metal surface will prevent the diffusion of ferrous ions, making the diffusion rate slower than iron oxidation.

As displayed in Fig. 7(a) and 9(c), the low-frequency region impedance and self-corrosion potential of the X80 steel at $10\text{ }^{\circ}\text{C}$ were $3.7\text{ k}\Omega\text{ cm}^2$ and -0.51706 V in silty soil containing 0.3% chloride ion, respectively. When the ion concentration increases to 1.5%, the impedance and the self-corrosion potential were $1.3\text{ k}\Omega\text{ cm}^2$ and -0.46855 V , respectively. That is to say, the decrease in the impedance magnitude and the increase in the self-corrosion potential commonly occur simultaneously (Ref 30). When the measured potential was higher than the self-corrosion potential, the measured current increased slowly, and the current began to increase rapidly after the transitional passivation area appears.

Chloride ions are used as a reductive media to cause corrosion of the steel specimens. The first situation for the occurrence of this corrosion thermodynamic behavior may be during the test process, a compact and dense oxide film is easily formed on the surface of the steel, which hinders the contact between the corrosive environment medium and the steel. However, due to the small radius of chloride ions and strong penetration force, it passes through the surface oxide film and reacts with the steel matrix to form complexes, destroying the original oxide film structure. The alternative situation may be the oxygen protective film and the adsorption film formed by the steel diminish the activity of the metal surface, but the

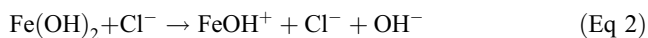
chloride ion in the corrosive environment has a more vital ability to be adsorbed by the metal, the chloride ion replaces passivating ions in adsorption. After the corrosion occurs, the corrosion product film will be formed on the steel surface. Its structure will gradually change from loose and porous to thin and dense, which will prevent the reducing medium in the soil from reaching the steel surface to some extent. Thus, the formation of corroded galvanic cells was affected, and the electrode process and depolarization process were blocked.

As the corrosion reaction progresses, the corrosion products on the steel surface continue to accumulate to produce a concentration difference. In order to reach equilibrium, the reducing medium in soil continues to be transported to the steel surface, and the corrosion product film with lower adhesion force makes the diffusion resistance of metal cations to the cathode smaller. In parallel, corrosive ions such as water molecules and chloride ions in the soil environment penetrate the product film through tiny pores of film to reach the steel interface and continue the iron oxidation process, that is, the chemical or electrochemical reaction between the corrosion product film and the corrosive anions adsorbed on it. The typical reaction formula is shown in the following Eq 2. As is clear from this formula, the chloride ions will not be consumed during the reaction, and the chloride ions released by the reaction continue to participate in the reaction to strengthen the activity of the local corrosion behavior. This suggested that the corrosion product film can effectively prevent direct contact between the soil corrosion environment and the metal matrix. However, as time goes by, the film gradually becomes invalid, and corrosion continues to occur. The soil corrosion environment with higher temperature and higher concentration of chloride ions also has a strong destructive effect on the structure of the product film on the steel surface, and it is more accessible to failure the shielding effect of the corrosion product film; that is, due to the effect of surface tension, the reducing medium will penetrate into the corrosion film, and since the adsorption of anions, the surface tension will be reduced. The peptization will cause cracks or clefts on the corrosion product film to cause damage (Ref 31). The rupture of the film affects the subsequent corrosion process. At the same time, pitting corrosion and hydrogen embrittlement reaction may occur on the steel surface. The noteworthy point is that, in the soil environment of high chloride ion concentration, due to the

Table 5 Electrochemical parameters taken from Tafel plots for X80 pipeline steel in the silty soil

Temperature	Cl- mass%	Ba mV	Bc mV	Icorr Amp/cm2	Ecorr Volts	Corrosion rate	
						mm/a	MPY
$-20\text{ }^{\circ}\text{C}$	0.3	135.53	114.93	8.64E-07	-0.58544	0.009213	0.36273
	0.5	378.21	204.42	1.47E-06	-0.6659	0.015721	0.61892
	1	289.73	210.49	1.83E-06	-0.56855	0.019548	0.76959
	1.5	391.01	200.94	1.76E-06	-0.56352	0.018806	0.74038
$-10\text{ }^{\circ}\text{C}$	0.3	172.32	148.23	7.41E-07	-0.57514	0.007907	0.31131
	0.5	336.82	189.58	2.25E-06	-0.56415	0.024019	0.94564
	1	1723.5	302.87	1.39E-05	-0.47865	0.1478	5.819
	1.5	1537.1	300.62	2.89E-05	-0.50533	0.30815	12.132
$10\text{ }^{\circ}\text{C}$	0.3	3722.6	360.95	4.09E-05	-0.51706	0.43638	17.18
	0.5	8027.9	339.82	6.10E-05	-0.47748	0.65048	25.609
	1	8546.7	423.9	8.16E-05	-0.52987	0.8702	34.26
	1.5	1.32E+07	224.91	4.72E-05	-0.46855	0.50326	19.813

effect of osmotic pressure, the transmission process of the reducing medium in the soil will also be accelerated.



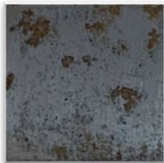
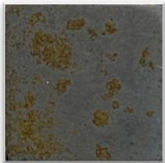


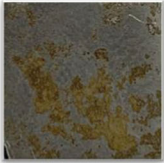


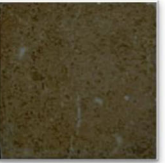
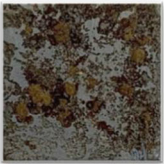



The occurrence of local corrosion behavior is reflected as the asymmetry of the anodic and cathodic Tafel slopes in the corrosion kinetic parameters, and the ratio will affect the alteration of the corrosion potential. When $B_a/B_c > 1$, the corrosion potential shifted in a positive direction; when $B_a/B_c < 1$, the corrosion potential shifted in a negative direction; and when $B_a/B_c = 1$, the corrosion potential changes insignificantly (Ref 10). As given in Table 5, in the concentration range of this test, the steels have local corrosion behavior and the corrosion potential changes positively. With the increase in the chloride ion content in the silty soil, when the temperature is $-20\text{ }^\circ\text{C}$, the self-corrosion potential first significantly decreases and then increases; when the soil temperature is $-10\text{ }^\circ\text{C}$, the self-corrosion potential first increases and then decreases. Their maximum values were achieved at 1.5 and 1% chloride ion concentrations in the soil environment, respectively. As can be seen from the blue curve in Fig. 9(a), the current remains low as the measured potential is above the self-corrosion potential until the potential is greater than -0.227 V ; due to the dissolution of iron ions, the current continues to increase at this moment. From the black curve in Fig. 9(b), as the potential is greater than the self-corrosion potential up to -0.325 V , the current increases rapidly, and an obvious transitional passivation stage occurs. The passivation film appears on the partial anode area of the steel work surface to prevent active dissolution. Simultaneously, as can be seen, the higher the temperature, the greater the value of the self-corrosion potential. At different temperatures, the change of the salinity results in the change of the corrosion potential, which increases the electrochemical activity of the steel.

With the increase in the chloride ion content in the silty soil at negative temperature, when the temperature is $-20\text{ }^\circ\text{C}$, the corrosion rate first increases and then decreases and reaches the maximum when the concentration is 1%; when the soil temperature is $-10\text{ }^\circ\text{C}$, the corrosion rate persistently increases. This is consistent with the above EIS results. This phenomenon is due to the stronger adsorption of chloride ions with higher concentration, and it is easier to accumulate on the defect positions of the corrosion product film on the steel surface to reduce the oxygen content in the soil near the steel surface, thus reducing the corrosion rate. Under freezing temperature of soil pore fluid, the corrosion rates at $-10\text{ }^\circ\text{C}$ are generally more prominent than $-20\text{ }^\circ\text{C}$. In the case of high corrosion rate, illustrating that the ions have enough interaction time and a shorter free collision path, that is, the possibility that the reactant and kinetic energy of the reactant will react with each other is increased. In a soil environment with a higher temperature, water and various corrosive ions are more active, reaching the steel interface faster, and the reducing mediums are transported faster.

3.3 The Corrosion Mechanism of X80 Steel in the Silty Soil at Various Temperatures

3.3.1 The Corrosion Morphology. The corrosion products of X80 steel under Cl^- test conditions consisted mainly of different types of iron oxides (Ref 32). The macroscopic corrosion morphologies of X80 steel in different soil temperature environments are shown in Table 6. It can be clearly seen that metallic luster is visible on the X80 steel surface in the silty soil with sub-zero temperature, and corrosion products appear locally on the X80 steel surface in the silty soil with low ion concentration. The yellow-brown corrosion products on the steel surface gradually increase in response to rising soil temperatures and ion concentrations. This is due to Fe^{2+} flows into the soil and oxidizes to Fe^{3+} . With the increase in the ion

Table 6 Macroscopic corrosion morphology of X80 steel at various temperatures

	0.3%	0.5%	1%	1.5%
$-20\text{ }^\circ\text{C}$				
$-10\text{ }^\circ\text{C}$				
$10\text{ }^\circ\text{C}$				

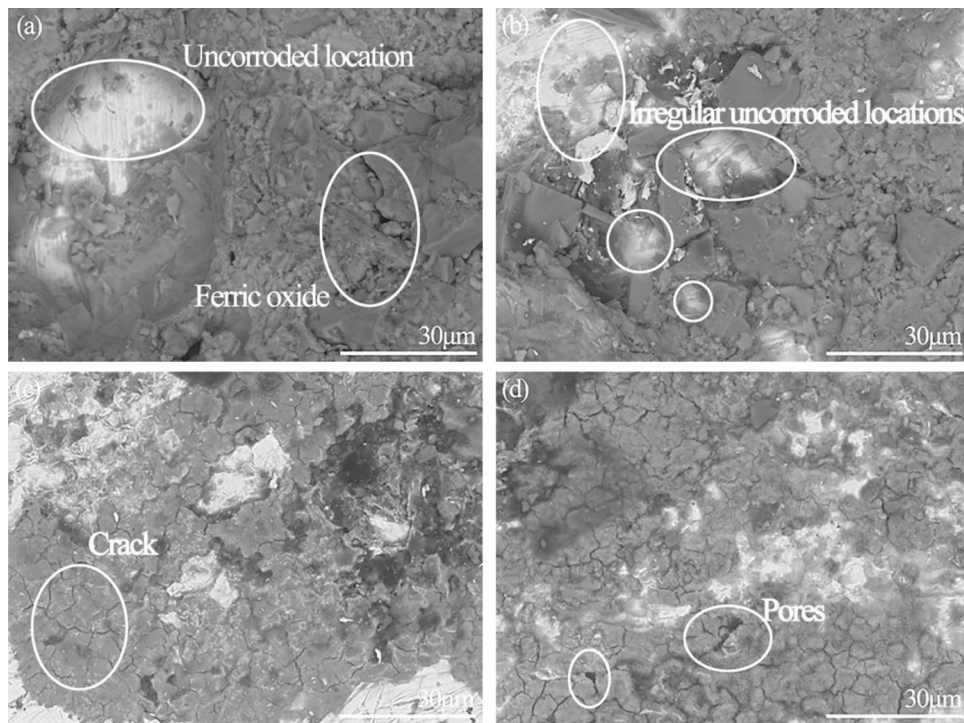


Fig. 10 Microscopic corrosion morphology of X80 steel at $-20\text{ }^{\circ}\text{C}$: (a) 0.3%; (b) 0.5%; (c) 1%; (d) 1.5%

concentration and temperature, the color of corrosion products on the steel surface is brighter, and the corrosion kinetics behavior is more significant. The steel surfaces are covered with black–brown Fe_3O_4 , red–brown Fe_2O_3 corrosion products and tightly adhered soil particles. When the soil environment temperature is -10 and $-20\text{ }^{\circ}\text{C}$, X80 steel surfaces have the most expansive corrosion area and the most severe corrosion behavior in soils containing 1.5 and 1% chloride ion concentration, respectively. This was in line with the above EIS results.

Figure 10 shows the surface corrosion morphologies of X80 steel after the potentiodynamic corrosion test with a soil temperature of $-20\text{ }^{\circ}\text{C}$. The corrosion products formed by deposition are accompanied by significant pores and cracks. Some of the deposition of corrosion product on the surface has apparent double-layer structure, and the primary layer still has traces of chemical–electrochemical corrosion. The relatively complete irregular elliptical uncorroded locations are usually seen in the localized corrosion. This is likely due to the pore fluid in soil particle phase transition to solid ice, and the ice formation hinders the progress of corrosion. The corrosion of steel specimens is pitting corrosion dominated. Corrosion product cluster coverage on the steel increases with increasing chloride ion concentration. Furthermore, its structure changes from loose to compact and then to looser. This is due to high-valent iron was reduced to low-valent iron, which flows into the soil as a relatively low iron ion concentration, the corrosion products are therefore looser (Ref 33). When the ion concentration was increased to 1%, the pitting corrosion is the most severe. This is consistent with the above PC results.

Microscopic morphologies of X80 steel in an environment with a soil temperature of $-10\text{ }^{\circ}\text{C}$ are shown in Fig. 11. As can be seen, a large number of soil particles adhered to the steel

surface and covered with a layer of loose corrosion products, this is particularly evident at low concentration. However, the steel surface is covered by a thick layer of corrosion products with cracks when the concentration increased to 1.5%. In parallel, it is possible to see that the corrosion products covered on the steel surface are discontinuous. The discontinuity is due to the corrosion reaction process is affected by the porous medium of soil (Ref 34). In the same soil environment at the freezing temperature of pore fluid, the steel specimen at $-10\text{ }^{\circ}\text{C}$ is consistent with $-20\text{ }^{\circ}\text{C}$, and there are irregular elliptical uncorroded regions that may be caused by the liquid–solid phase transition hindering the reducing medium reached the steel surface. Contrasted with $-20\text{ }^{\circ}\text{C}$, the corrosion layer has more cracks and pores at $-10\text{ }^{\circ}\text{C}$, making it easier for the reducing medium in the soil to reach the steel interface through the defects in the layer corrosion is more significant.

SEM analysis was performed to contrast the detailed micromorphology of the X80 steel in various soil environments. Microscopic morphologies of X80 steel in the silty soil with a soil temperature of $10\text{ }^{\circ}\text{C}$ are shown in Fig. 12. As a consequence of the porosity of the rust layer on the steel surface, there are a large number of corrosion pits and cracks on the rust layer after contact with the pore water. The smaller the salt content, the more the corrosion pits exist. However, with the increase in the salt content, the corrosion pits are eroded and deepened until they form a larger corrosion region, and the cracks gradually expand to intersect. As shown in Fig. 12, the degree of corrosion on the steel surface and the number of corrosion products increased with increasing soil temperature. The irregular pits gradually become larger, deeper and further extended. Compared with the soil environment under the freezing temperature of the pore fluid, there are few irregular uncorroded areas in the local corrosion range in the positive

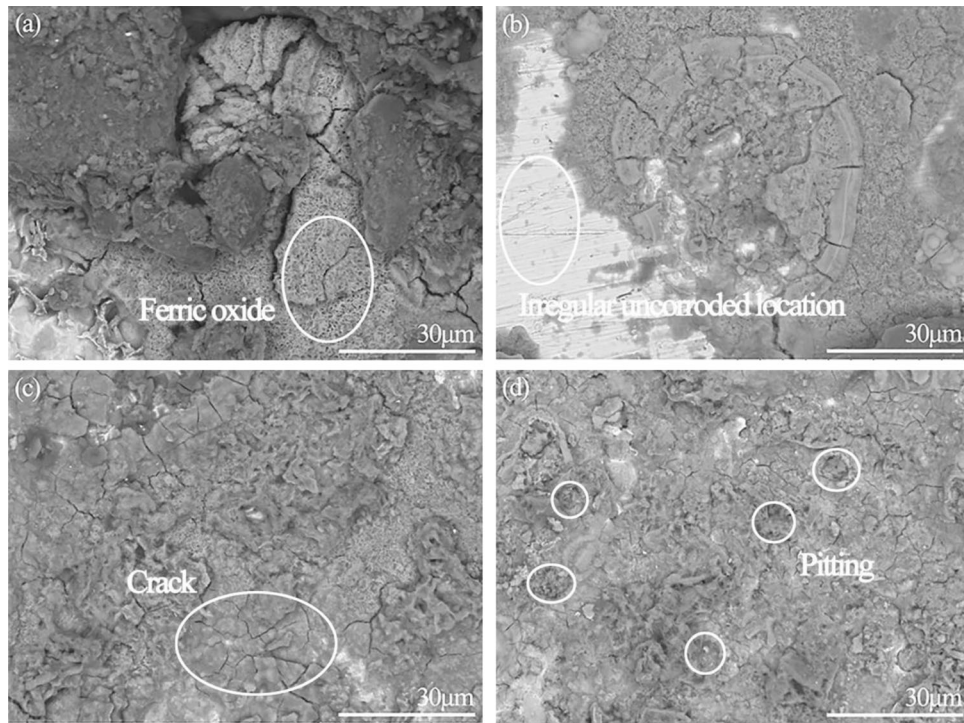


Fig. 11 Microscopic corrosion morphology of X80 steel at $-10\text{ }^{\circ}\text{C}$: (a) 0.3%; (b) 0.5%; (c) 1%; (d) 1.5%

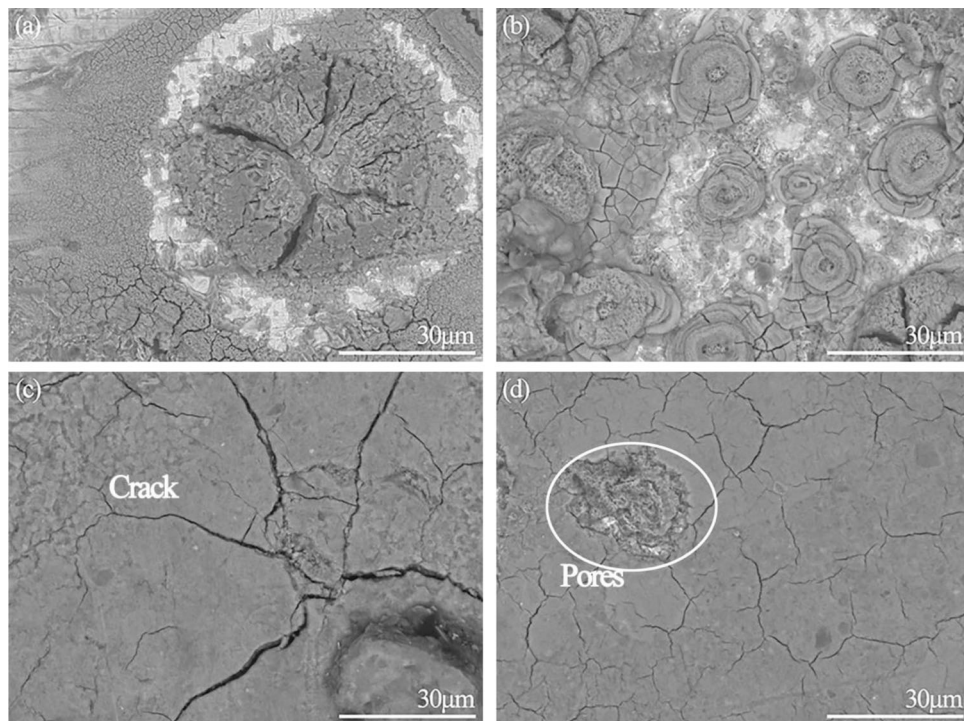


Fig. 12 Microscopic corrosion morphology of X80 steel at $10\text{ }^{\circ}\text{C}$: (a) 0.3%; (b) 0.5%; (c) 1%; (d) 1.5%

temperature soil environment. When the soil temperature increases, the current density generated by the better soil conductivity increases, and the exothermic process is evident, which causes the rust layer to produce a dehydration reaction. Clear trends can be seen, and the rust layer on the steel surface is relatively dry at the positive temperature.

3.3.2 The Corrosion Products. EDS scan of the local area in the above microscopic morphology and the elemental analysis is shown in Fig 13, 14 and 15, respectively. Among them, Fe and O elements originate from the corrosion products formed during the corrosion process, and their maximum

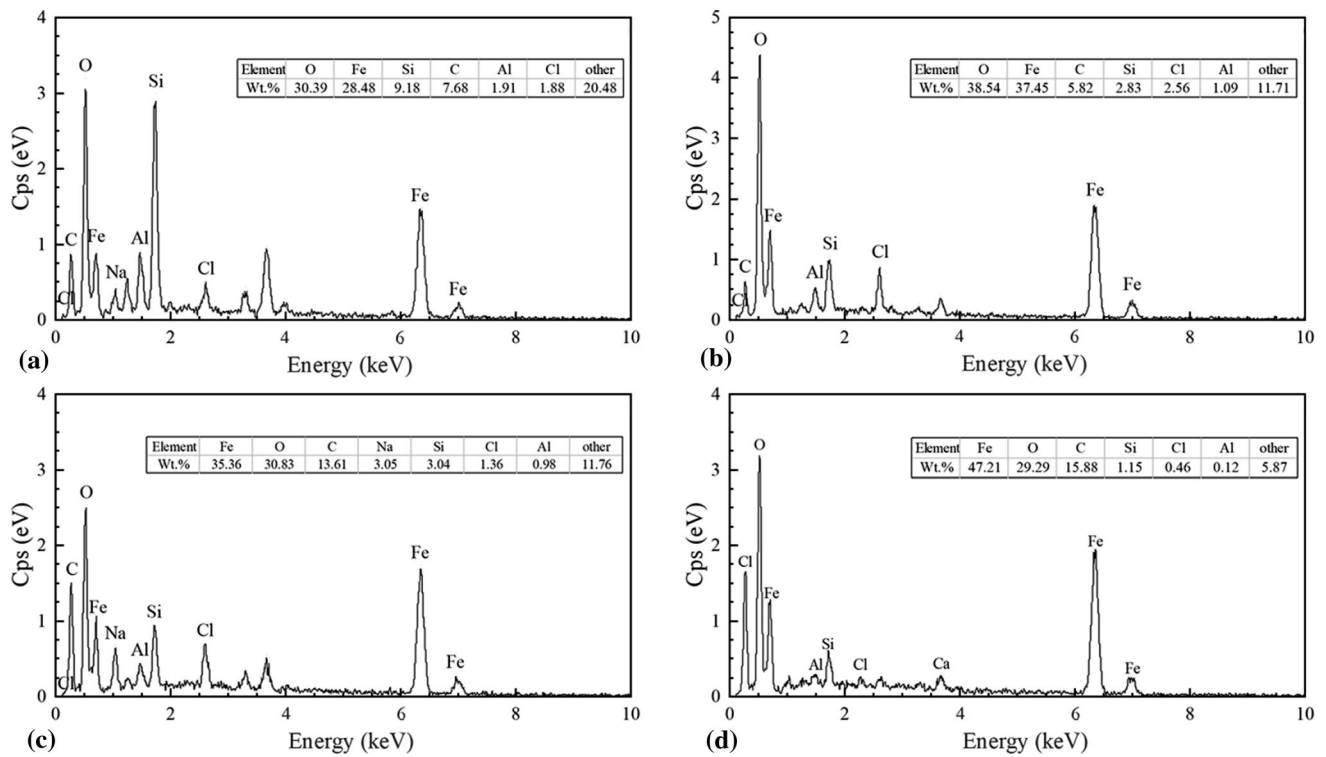


Fig. 13 EDS spectra of the rust layers at $-20\text{ }^{\circ}\text{C}$: (a) 0.3%; (b) 0.5%; (c) 1%; (d) 1.5%

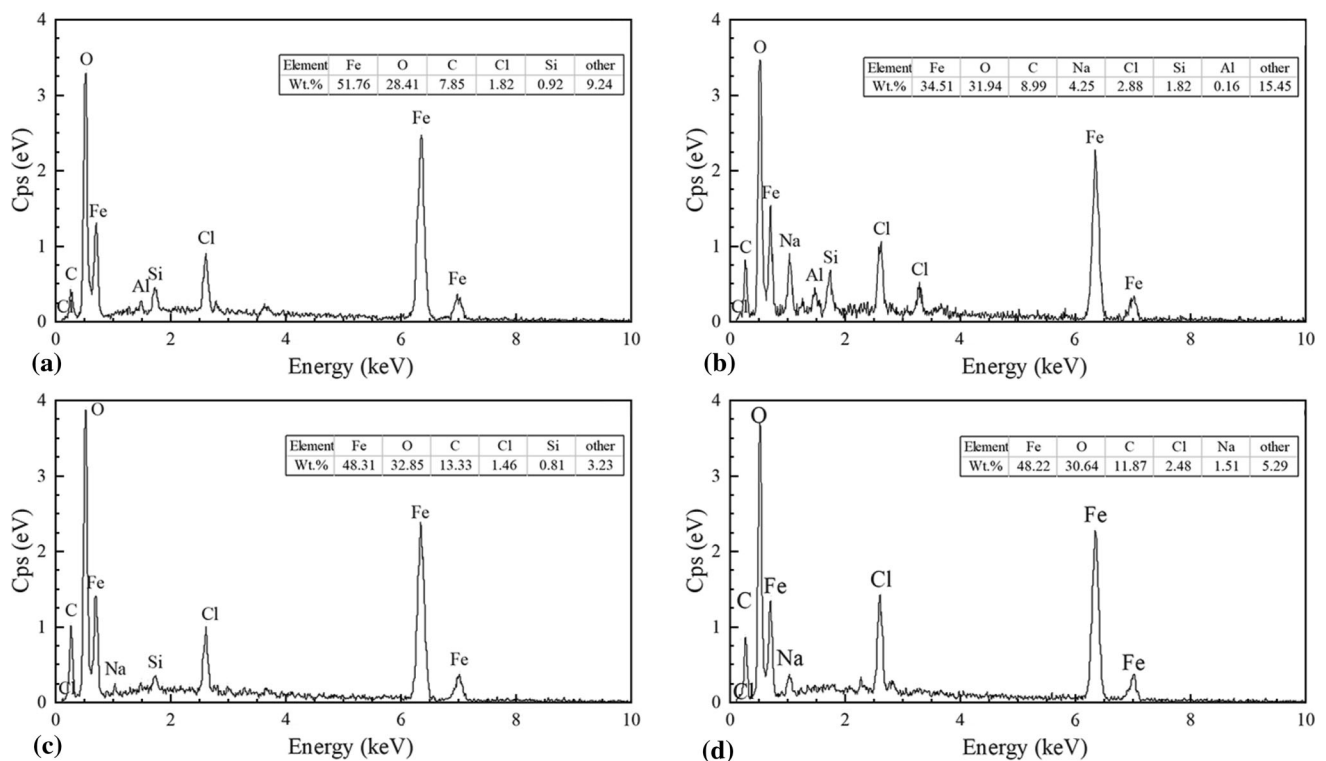


Fig. 14 EDS spectra of the rust layers at $-10\text{ }^{\circ}\text{C}$: (a) 0.3%; (b) 0.5%; (c) 1%; (d) 1.5%

content indicates that iron oxide is the main component of the corrosion product. The content of iron oxide increases with increasing the soil environment temperature. The Na and Cl

elements originate from NaCl which simulates the sedimentation of salt in the test silty soil. The Si and Al elements may originate from the SEM sample stage. In the soil environment at

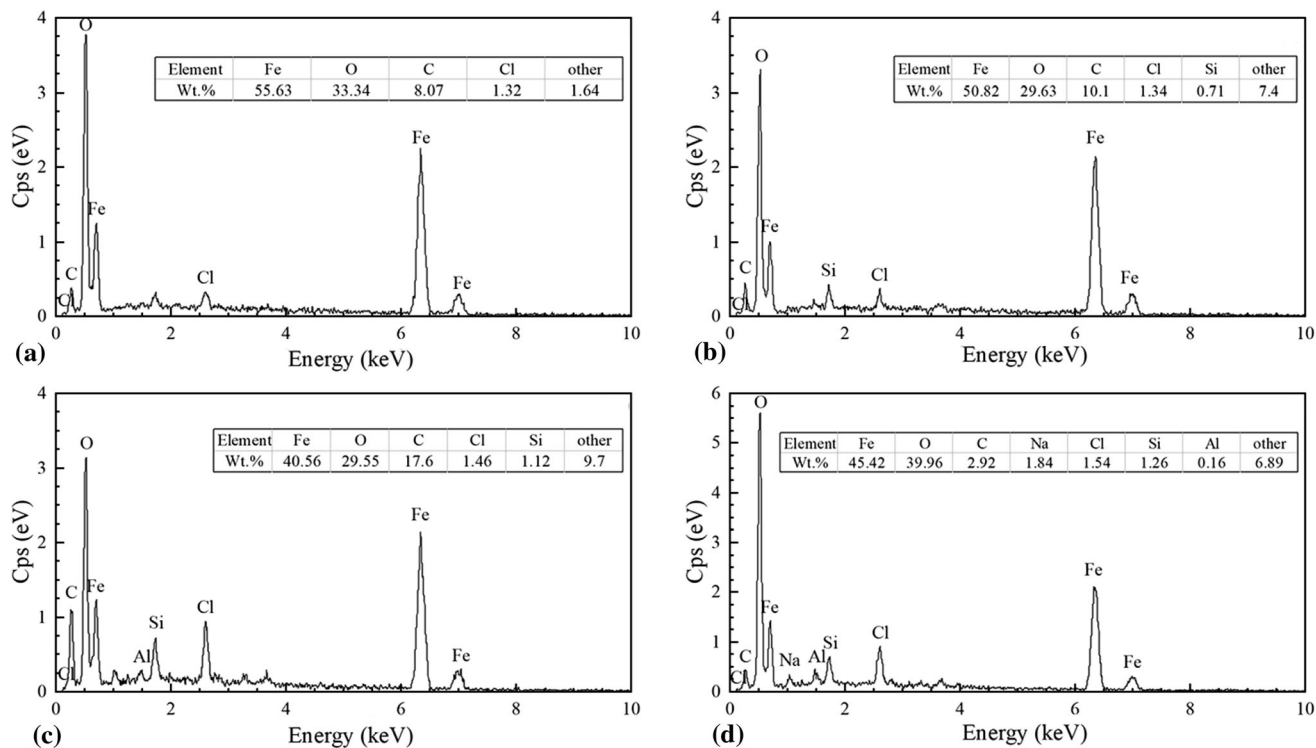


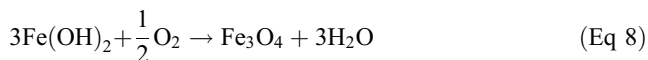
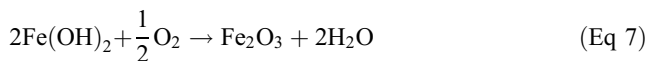
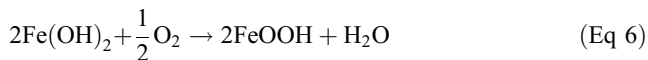
Fig. 15 EDS spectra of the rust layers at 10°C: (a) 0.3%; (b) 0.5%; (c) 1%; (d) 1.5%

the freezing temperature of pore fluid, the content of elements from the corrosive environment in the scanning results of $-10\text{ }^\circ\text{C}$ is large, indicating that the reducing medium penetrates into the rust layer. This is consistent with the above electrochemical test results.

In different soil corrosion settings, the major reaction process of the steel is:

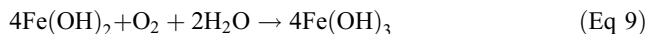


When the steel in sub-zero temperature (anoxic) soil corrosion settings, the soil body is in a freezing process, and the dissolved oxygen level is relatively low, which blocks the oxygen diffusion path and depolarization.

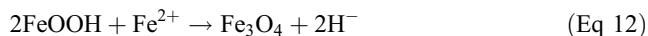


When the steel in positive temperature soil corrosion settings:

$\text{Fe}(\text{OH})_2$ is unstable and easily oxidized to $\text{Fe}(\text{OH})_3$



Due to the high current density, the exothermic process is significant, dehydration reaction occurs, and the rust layer is relatively dry (Ref 35).



3.3.3 Summary. Unsaturated soil is a multinomial mixture of solid, liquid, gas and shrink wrap film phase. Its liquid phase is affected by the adsorption on the surface charged soil particles and the capillary force. Under negative temperature conditions, part of the free water flowing in the soil micropores will cause deformation of the soil structure, such as cold shrinkage, frost heave and salt swelling due to icing. When the soil temperature is negative, the solid ice gradually precipitates out of the pore solution. However, simultaneously there is still a certain amount of unfrozen water in the soil pore structure (Ref 36-38). The unfrozen water in the soil pores spaces has a substantial impact on the redistribution of water and salt (the migration and aggregation of water and salt) (Ref 39, 40). The precipitation of solid ice in the soil pores will impede the electrical pathways, but it is precisely for that the presence of unfrozen water plays an essential role in the mass transfer process of the corrosive medium at the soil-steel interface continues to occur. A review of existing research shows that when the temperature of the soil containing chloride ions is between -20 and $20\text{ }^\circ\text{C}$, only the liquid-solid phase transition occurs in the soil; that is, when the chloride ion concentration increases, the content of unfrozen water in the soil will increase, and it has an inhibitory effect on the icing. However, the change

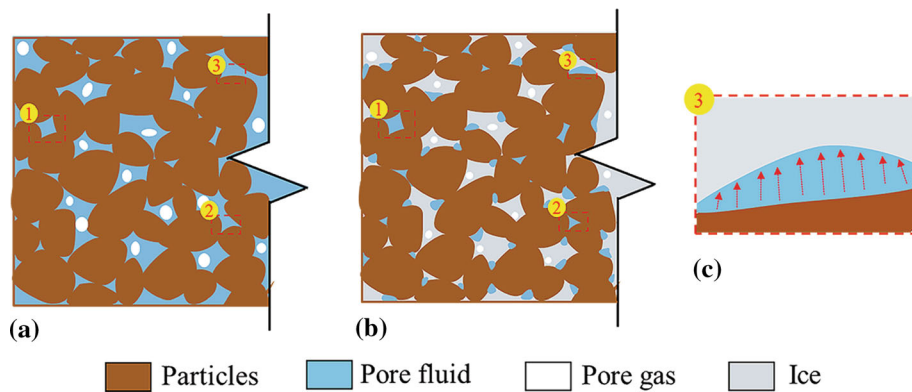


Fig. 16 Schematic diagram of medium migration during soil freezing: (a) before freezing; (b) after freezing; (c) unfrozen water migration

of chloride ion concentration in the soil within the above-mentioned temperature range has less impact on the structural change of the soil (Ref 41-43).

TENG J divides the freezing characteristic curve of silt soil into three stages (Ref 44): The first stage is when the temperature is between -5 and 0 °C, the pore water content in the soil almost no changes; that is, there is almost no phase transition to precipitate solid ice. The second stage is when the temperature gradually drops to -5 °C, the unfrozen water content decreases rapidly, and the liquid water phase in the pores of the solid soil particles changes into ice. In the third stage, as the temperature decreases, the unfrozen water content slowly decreases. The remaining liquid water is mainly the water film around the soil particles.

Figure 16 shows a schematic diagram of medium migration during soil freezing. Sodium chloride-containing soil specimens that have been in a negative temperature environment for long times will appear as the pore fluid gradually phases into solid ice. Meanwhile, the solid particles and pore gas are squeezed to introduce some minor deformations, resulting in supercooling of some pore water. The reasons for this phenomenon can be roughly divided into three situations: In region ①, the pore fluid is surrounded by solid soil particles and is not prone to phase transition, and as the freezing time increases, the surrounding solid particles can act as the condensation nuclei required in the process of pore fluid freezing into ice, so that the pore fluid surrounded by it undergoes a phase transition. In region ②, the pore fluid is in a free state before freezing. Through freezing time, the surrounding soil solid particles are squeezed by the solid ice formed by the phase transition to gradually form a sealing zone, causing this part of the pore fluid difficult to phase transition. The region ③ represents the migration process of unfrozen water. This area of the soil pore fluid is in direct contact with the solid ice. At this point, the pore fluid is prone to phase transition and gradually phases into ice.

At sub-zero temperature, the test silty soil has a low temperature, poor electrical conductivity and high charge transfer resistance. The pores of the test soil contain liquid water, ice and air. As the test temperature decreases, ice is gradually precipitated from the pore fluid of the silty soil containing chloride ions, which hampers the flow of current and changes the path of the electrical channel. Simultaneously, the liquid–solid phase transition causes a lack of oxygen around the test steel surface, forming an anoxic corrosive environment. In a hypoxic microenvironment, the number of corrosion sedi-

ments formed on the steel surface decreases and the corrosion rate decreases. At positive temperature, the pores of the soil contain adsorbed water, liquid film water, capillary water and gravitational water. The pore water is in a stable flow state, with excellent charge flow and conductivity. Most of the current is conducted through the pore fluid, and the consistency of the electrical channels has less influence.

4. Conclusion

The corrosion thermodynamics and kinetics behaviors of X80 steel were experimentally investigated in the silty soil containing chloride ion under different temperatures. The main conclusions drawn within the concentration range of this test are as follows:

- (1) The presence of chloride ions in the silty soil increases the corrosion thermodynamics of X80 steel. The content of unfrozen water in the soil increases with the growth of chloride ion concentration, which hinders the phase transition of pore fluid. At -10 °C, the corrosion rate increases with the increase in the chloride ion concentration. At -20 °C, the corrosion rate first increases and then decreases with increasing concentration and reaches the maximum at 1% content.
- (2) The cathodic reaction of soil electrolyte at negative temperature effects would have less influence. The anodic polarization curve at -10 °C occurs passivation at 0.5-1.5% concentration. At -20 °C, the anodic polarization curve occurs passivation zone at 1% concentration, and when the concentration increases to 1.5%, the corrosion behavior transforms to controlled by activation polarization.
- (3) In contrast to the test results of a positive temperature corrosion environment, it is concluded that the impedance spectrum radius in the low-frequency region is larger at negative temperature. The lower the test temperature, the lower the unfrozen water content in the silty soil, the worse the conductivity will be, forming an anoxic corrosion environment. The negative temperature will reduce the corrosion kinetic properties of steel.
- (4) The composition of corrosion product included mainly iron oxides. With ion concentration and temperature increase in the soil environment, the color of corrosion

products on the steel surface appears brighter. The steel corroded surface were present irregular elliptical uncorroded areas at pore water freezing temperature that may be caused by the liquid–solid phase transition hindering the reducing medium transportation. When in a positive temperature soil environment, the current density is high. The exothermic process is obvious, and the rust layer is relatively dry.

Acknowledgment

The authors gratefully acknowledge financial support from the National Natural Science Foundation of China (No. 41807256), the Open Research Fund of State Key Laboratory of Geomechanics and Geotechnical Engineering, Institute of Rock and Soil Mechanics, Chinese Academy of Sciences (No. Z017003), the Ph.D research launch project of Jinzhong University, the Scientific and technological innovation projects of colleges and universities in Shanxi Province, and the Opening Project of Sichuan University of Science and Engineering, Material Corrosion and Protection Key Laboratory of Sichuan province (No. 2020CL13).

Conflict of interest

No conflict of interest exists in the submission of this manuscript, and the manuscript is approved by all authors for publication.

References

- W. Wu, Y. Li, G.X. Cheng, H. Zhang and J. Kang, Dynamic Safety Assessment of Oil and Gas Pipeline Containing Internal Corrosion Defect using Probability Theory and Possibility Theory, *Eng. Fail. Anal.*, 2019, **98**, p 156–166.
- R. Pourazizi, M.A. Mohtadi-Bonab and J.A. Szpunar, Role of Texture and Inclusions on the Failure of An API X70 Pipeline Steel at Different Service Environments, *Mater. Charact.*, 2020, **164**, p 110330.
- M.E.A. Ben Seghier, B. Keshtegar, M. Taleb-Berrouane, R. Abbassi and N.T. Trung, Advanced Intelligence Frameworks for Predicting Maximum Pitting Corrosion Depth in Oil and Gas Pipelines, *Process Saf. Environ. Prot.*, 2021, **147**, p 818–833.
- T.Y. Wang, D.Y. Xu, L.N. Qu, J.W. Fu and Z.L. Li, An Extension Approach to Estimate Soil Corrosivity for Buried Pipelines, *Int. J. Press. Vess. Pip.*, 2021, **192**, p 104413.
- Y.M. Su, F. Xie and D. Wang, Synergistic Effect of Factors Influencing the External Corrosion of Heavy Oil Pipelines in Reed Pond Soil, *J. Mater. Eng. Perform.*, 2021, **30**(5), p 3556–3567.
- S.X. Wang, X.L. Yin, H. Zhang, D.X. Liu and N. Du, Coupling Effects of pH and Dissolved Oxygen on the Corrosion Behavior and Mechanism of X80 Steel in Acidic Soil Simulated Solution, *Materials (Basel)*, 2019, **12**(19), p 3175.
- J. Eid, H. Takenouti, B. Ait Saadi and S. Taibi, Electrochemical Studies of Steel Rebar Corrosion in Clay: Application to a Raw Earth Concrete, *Corros. Sci.*, 2020, **168**, p 108556.
- J.S. Li, Y.F. Zhou, Q.M. Wang, Q. Xue and C.S. Poon, Development of a Novel Binder using Lime and Incinerated Sewage Sludge Ash to Stabilize/Solidify Contaminated Marine Sediments with High Water Content as a Fill Material, *J. Mater. Civ. Eng.*, 2019, **31**(10), p 04019245.
- H.W. Liu, Y.N. Dai and Y.F. Cheng, Corrosion of Underground Pipelines in Clay Soil with Varied Soil Layer Thicknesses and Aerations, *Arab. J. Chem.*, 2020, **13**(2), p 3601–3614.
- Q.Y. Qin, B.X. Wei, Y.L. Bai, Q. Fu, J. Xu, C. Sun, C. Wang and Z.Y. Wang, Effect of Alternating Current Frequency on Corrosion Behavior of X80 Pipeline Steel in Coastal Saline Soil, *Eng. Fail. Anal.*, 2021, **120**, p 105065.
- B. Liu, M.H. Sun, F.Y. Lu, C.W. Du and X.G. Li, Study of Biofilm-Influenced Corrosion on X80 Pipeline Steel by a Nitrate-Reducing Bacterium, *Bacillus Cereus*, in Artificial Beijing Soil, *Colloids Surfaces B Biointerfaces.*, 2021, **197**, p 111356.
- Y. Huang, D. Xu, L.Y. Huang, Y.T. Lou, J.B. Muhadesi, H.C. Qian, E.Z. Zhou, B.J. Wang, X.T. Li, Z. Jiang, S.J. Liu, D.W. Zhang and C.Y. Jiang, Responses of Soil Microbiome to Steel Corrosion, *NPJ Biofilms Microbiomes*, 2021, **7**(1), p 6.
- X.H. Wang, Z.Q. Wang, Y.C. Chen, X.T. Song and C. Xu, Research on the Corrosion Behavior of X70 Pipeline Steel under Coupling Effect of AC + DC and Stress, *J. Mater. Eng. Perform.*, 2019, **28**(2), p 1958–1968.
- S. Karthick, S. Muralidharan and V. Saraswathy, Corrosion Performance of Mild Steel and Galvanized Iron in Clay Soil Environment, *Arab. J. Chem.*, 2020, **13**(1), p 3301–3318.
- Q.K. Zhang, S.L. Larson, J.H. Ballard, X.C. Zhu, H.M. Knotek-Smith and F.X. Han, Uranium Metal Corrosion in Soils with Different Soil Moisture Regimes, *Corros. Sci.*, 2021, **179**, p 109138.
- Q. Fu, J. Xu, B.X. Wei, Q.Y. Qin, L.Q. Gao, Y.L. Bai, C.K. Yu and C. Sun, The Effect of Nitrate Reducing Bacteria on the Corrosion Behavior of X80 Pipeline Steel in the Soil Extract Solution of Shenyang, *Int. J. Press. Vessel. Pip.*, 2021, **190**, p 104313.
- M. Wasim, S. Shoaib, N.M. Mubarak and A.M. Asiri, Factors Influencing Corrosion of Metal Pipes in Soils, *Environ. Chem. Lett.*, 2018, **16**(3), p 861–879.
- B.X. Wei, J. Xu, Q. Fu, Q.Y. Qin, Y.L. Bai, C. Sun, C. Wang, Z.Y. Wang and W. Ke, Effect of Sulfate-Reducing Bacteria on Corrosion of X80 Pipeline Steel under Disbonded Coating in a Red Soil Solution, *J. Mater. Sci. Technol.*, 2021, **87**, p 1–17.
- Q.L. Zhang, M.H. Xue, D. Wang, Y. Zi and J. Zhou, Effect of CO₃²⁻ Concentration on the Corrosion Behavior of X80 Pipeline Steel in Simulated Soil Solution, *Int. J. Electrochem. Sci.*, 2020, **15**, p 4592–4601.
- Y.H. Wu, S.X. Luo and Q.S. Mou, Influence of Temperature on the Corrosion Behavior of X80 Steel in an Acidic Soil Environment, *Int. J. Electrochem. Sci.*, 2020, **15**, p 576–586.
- Minimum temperature data in Taiyuan City, Shanxi Province, China. China Meteorological Data Service Centre, <http://data.cma.cn>. Accessed 5 Mar 2021 (2021)
- Standard for engineering classification of soil, GB/T 50145-2007, p 6–7. N. H. R. Institute, China Planning Press, Beijing, (2008). (in Chinese)
- J. Qiu, Y.H. Li, Y. Xu, A.J. Wu and D.D. Macdonald, Effect of Temperature on Corrosion of Carbon Steel in Simulated Concrete Pore Solution under Anoxic Conditions, *Corros. Sci.*, 2020, **175**, p 108886.
- M.C. Yan, C. Sun, J.H. Dong, J. Xu and W. Ke, Electrochemical Investigation on Steel Corrosion in Iron-Rich Clay, *Corros. Sci.*, 2015, **97**, p 62–73.
- L.M. Quej-Ake, A. Contreras, H.B. Liu, J.L. Alamilla and E. Sosa, Assessment on External Corrosion Rates for API Pipeline Steels Exposed to Acidic Sand-Clay Soil, *Anti-Corros. Methods Mater.*, 2018, **65**(3), p 281–291.
- N. Sato, A Theory for Breakdown of Anodic Oxide Films on Metals, *Electrochim. Acta.*, 1971, **16**, p 1683–1692.
- Y.G. Chen, L.N. Liu, W.M. Ye, Y.J. Cui and D.B. Wu, Deterioration of Swelling Pressure of Compacted Gaomiaozi Bentonite Induced by Heat Combined with Hyperalkaline Conditions, *Soils Found.*, 2019, **59**(6), p 2254–2264.
- Y.G. Chen, X.X. Dong, X.D. Zhang, W.M. Ye and Y.J. Cui, Cyclic Thermal and Saline Effects on the Swelling Pressure of Densely Compacted Gaomiaozi Bentonite, *Eng. Geol.*, 2019, **255**, p 37–47.
- T. Kosec, Z. Qin, J. Chen, A. Legat and D.W. Shoesmith, Copper Corrosion in Bentonite/Saline Groundwater Solution: Effects of Solution and Bentonite Chemistry, *Corros. Sci.*, 2015, **90**, p 248–258.
- D. Ding, Y. Zhang, X.B. Yu, B.L. Fang, J.P. Guo, J. Li, L. Liu, C.W. Du and Z. Liu, Effects of Environmental Factors on Corrosion Behavior of High-Silicon Cast Iron in Shanxi Soil Medium, *Anti-Corros. Methods Mater.*, 2018, **65**(5), p 538–546.
- H.C. Ma, B. Zhao, Z.Y. Liu, C.W. Du and B.A. Shou, Local Chemistry–Electrochemistry and Stress Corrosion Susceptibility of X80 Steel Below Disbonded Coating in Acidic Soil Environment under Cathodic Protection, *Constr. Build. Mater.*, 2020, **243**, p 118203.

32. F.N. Sun, R.Z. Xie, B. He, Z.W. Chen, X.L. Bai and P.J. Han, The Initial Stage Corrosion of X80 Steel in Saturated Sandy Soil Containing Cl^- and SO_4^{2-} , *Int. J. Electrochem. Sci.*, 2021, **16**, p 150878.
33. Z.M. You, Y.M. Lai, H.Y. Zeng and Y.H. Yang, Influence of Water and Sodium Chloride Content on Corrosion Behavior of Cast Iron In Silty Clay, *Constr. Build. Mater.*, 2020, **238**, p 117762.
34. B. He, C.H. Lu, P.J. Han and X.H. Bai, Short-Term Electrochemical Corrosion Behavior of Pipeline Steel in Saline Sandy Environments, *Eng. Fail. Anal.*, 2016, **59**, p 410–418.
35. Z.C. Xu, Y.X. Du, R.Z. Qin and H. Zhang, Study of Corrosion Behavior of X80 Steel in Clay Soil with Different Water Contents Under HVDC Interference, *Int. J. Electrochem. Sci.*, 2020, **15**, p 3935–3954.
36. L.M. Kong, Y.S. Wang, W.J. Sun and J.L. Qi, Influence of Plasticity on Unfrozen Water Content of Frozen Soils as Determined by Nuclear Magnetic Resonance, *Cold Reg. Sci. Technol.*, 2020, **172**, p 102993.
37. M.Y. Zhang, X.Y. Zhang, J.G. Lu, W.S. Pei and C. Wang, Analysis of Volumetric Unfrozen Water Contents in Freezing Soils, *Exp. Heat Transf.*, 2019, **32**(5), p 426–438.
38. G.J. Hu, L. Zhao, X.F. Zhu, X.D. Wu, T.H. Wu, R. Li, C.W. Xie and J.M. Hao, Review of Algorithms and Parameterizations to Determine Unfrozen Water Content in Frozen Soil, *Geoderma*, 2020, **368**, p 114277.
39. J. Zhang, Y.M. Lai, J.F. Li and Y.H. Zhao, Study on the Influence of Hydro-Thermal-Salt-Mechanical Interaction in Saturated Frozen Sulfate Saline Soil Based on Crystallization Kinetics, *Int. J. Heat Mass Tran.*, 2020, **146**, p 118868.
40. Z.A. Xiao, Z.R. Hou, L.Z. Zhu and X.Q. Dong, Experimental investigation of the influence of salt on the phase transition temperature in saline soil, *Cold Reg. Sci. Technol.*, 2021, **183**, p 103229.
41. J.P. Liu, P. Yang and Z. JoeyYang, Electrical Properties of Frozen Saline Clay and Their Relationship with Unfrozen Water Content, *Cold Reg. Sci. Technol.*, 2020, **178**, p 103127.
42. J.P. Liu, P. Yang, L. Li and T. Zhang, Characterizing Pore-Size Distribution of a Chloride Silt Soil During Freeze-Thaw Process Using Nuclear Magnetic Resonance Relaxometry, *Soil Sci. Soc. Am. J.*, 2020, **84**(5), p 1577–1591.
43. Y. Zhang, Z.H. Yang, J.K. Liu and J.H. Fang, Impact of Cooling on Shear Strength of High Salinity Soils, *Cold Reg. Sci. Technol.*, 2017, **141**, p 122–130.
44. J.D. Teng, J.Y. Kou, X.D. Yan, S. Zhang and D.C. Sheng, Parameterization of Soil Freezing Characteristic Curve for Unsaturated Soils, *Cold Reg. Sci. Technol.*, 2020, **170**, p 102928.

Publisher's Note Springer Nature remains neutral with regard to jurisdictional claims in published maps and institutional affiliations.